RESOLVENT-BASED DESIGN AND EXPERIMENTAL TESTING OF POROUS MATERIALS FOR PASSIVE TURBULENCE CONTROL

Andrew Chavarin
Aerospace and Mechanical Engineering
University of Southern California
achavari@usc.edu

Christoph Efstathiou
Aerospace and Mechanical Engineering
University of Southern California
efstathi@usc.edu

Shilpa Vijay
Aerospace and Mechanical Engineering
University of Southern California
shilpavi@usc.edu

Mitul Luhar
Aerospace and Mechanical Engineering
University of Southern California
luhar@usc.edu

ABSTRACT

An extended version of the resolvent formulation is used to evaluate the effect of anisotropic porous materials on turbulent channel flow. The effect of these porous substrates is introduced into the governing equations via a generalized version of Darcy's law. Model predictions show that materials with high streamwise permeability and low wall-normal permeability ($\phi_{xy} = k_{xx}/k_{yy} \gg 1$) can suppress resolvent modes resembling the energetic near-wall cycle. Based on these predictions, two anisotropic porous substrates with $\phi_{xy} \approx 8$ and $\phi_{xy} \approx 1/8$ were designed and fabricated for water channel tests. PIV measurements were used to compute mean turbulence statistics, and to educe coherent structure. The Reynolds shear stress profiles did not show evidence of friction reduction over the streamwise-permeable substrate. However, the coherent structures extracted via POD analysis showed qualitative agreement with model predictions.

INTRODUCTION

Functional surfaces such as sharkskin-inspired riblets and denticles are some of the simplest and most effective control techniques tested thus far for turbulent friction reduction. Appropriately shaped and sized riblets have shown the ability to reduce drag up to 10% in laboratory experiments and up to 2% in real world conditions (Luchini *et al.*, 1991; Robert, 1992; Walsh & Lindemann, 1984; Garcia-Mayoral & Jimenez, 2011). It is generally accepted that the drag-reducing ability of such surfaces arises from their anisotropy: they offer much less resistance to streamwise flows compared to spanwise flows (Luchini *et al.*, 1991). The mean flow in the streamwise direction is essentially unimpeded within the riblet grooves, generating high interfacial slip. However, cross-flows arising from turbulence are blocked by the riblets and pushed further from the wall. This blocking effect weakens the streamwise vortices associated with the energetic near-wall (NW) cycle, and reduces turbulent velocity fluctuations and Reynolds stresses above the riblets (Choi *et al.*, 1993). Skin friction reduction initially increases with increasing riblet spacing and height. However, above a certain size threshold, performance deteriorates dramatically. Early studies attributed this deterioration of performance to the NW streamwise vortices lodging within the riblet grooves (Choi *et al.*, 1993; Lee & Lee, 2001). More recently, Garcia-Mayoral & Jimenez (2011) showed that a Kelvin-Helmholtz-type instability may also contribute to the deterioration of performance.

Recent theoretical efforts and numerical simulations (Abderrahaman-Elena & García-Mayoral, 2017; Rosti *et al.*, 2018; Gómez-de Segura *et al.*, 2018) suggest that anisotropic porous substrates with streamwise permeability (k_{xx}) that is higher than wall-normal permeability (k_{yy}) can have a similar effect as riblets, with reported friction drag reductions as high as 18% for $\phi_{xy} = k_{xx}/k_{yy} \gg 1$. With anisotropic porous materials, high porosity and streamwise permeability contribute to a substantial interfacial slip velocity, while low wall-normal permeability limits turbulence penetration into the porous substrate. Similar to flow over riblets, a Kelvin-Helmholtz instability is also predicted to arise for materials with high wall-normal permeability (Abderrahaman-Elena & García-Mayoral, 2017; Gómez-de Segura *et al.*, 2018). The effect of anisotropic porous materials has been characterized in recent channel flow experiments by Suga *et al.* (2018), though the materials tested did not have $\phi_{xy} > 1$.

In this work, we seek to design and fabricate anisotropic porous materials that have the potential to reduction skin friction, and to test these materials in laboratory experiments. An extended version of the resolvent framework (McKeon & Sharma, 2010) is used to predict the effect of porous materials with varying anisotropic permeability on flow structures resembling the NW cycle, and to test for the emergence of spanwise rollers resembling Kelvin-Helmholtz vortices. Materials predicted to be effective at suppressing the NW cycle are then fabricated and tested in benchtop channel flow experiments.

METHODS

Extended Resolvent Formulation

We utilize a modified version of the resolvent formulation proposed by McKeon & Sharma (2010) to design anisotropic porous materials for passive turbulence control.

For wall-bounded turbulent flows, the resolvent formulation interprets the Fourier-transformed Navier-Stokes equations as a forcing-response system: the nonlinear convective terms are interpreted as the forcing that acts on the remaining linear terms to give rise to a velocity and pressure response. For each wavenumber-frequency combination $\mathbf{k} = (\kappa_x, \kappa_z, \omega)$, a gain-based singular value decomposition of the forcing-response transfer function—the resolvent operator—yields a set of highly amplified velocity and pressure modes. These response modes ('resolvent modes') are flow structures with streamwise and spanwise wavelength $\lambda_x = 2\pi/\kappa_x$ and $\lambda_z = 2\pi/\kappa_z$, respectively, traveling at speed $c = \omega/\kappa_x$. Previous work shows that specific high-gain response modes can serve as useful models for energetic structures such as the NW cycle. These resolvent modes can therefore serve as building blocks for the design and optimization of active and passive control strategies (Luhar *et al.*, 2014; Chavarin & Luhar, 2018).

To account for the presence of an anisotropic porous medium, the resolvent framework is extended to the volume-averaged Navier-Stokes (VANS) equations, in which the effect of the porous substrate appears through a generalized version of Darcys law (Breugem *et al.*, 2006):

$$\frac{\partial \mathbf{u}}{\partial t} + \frac{1}{\varepsilon}\nabla\cdot\left(\varepsilon\mathbf{u}\mathbf{u}\right) = -\nabla p + \frac{1}{\varepsilon Re_\tau}\nabla^2(\varepsilon\mathbf{u}) - \frac{\mathbf{K}^{-1}}{Re_\tau Da}\varepsilon\mathbf{u}. \tag{1}$$

Here, $\mathbf{u}$ is velocity, p is pressure, ε is the porosity, $\mathbf{K} = \mathrm{diag}(k_{xx}, k_{yy}, k_{zz})$ is the assumed (diagonal) permeability tensor, Re_τ is the friction Reynolds number, and Da is the Darcy number. The unobstructed fluid domain is characterized by infinite permeability. For this region, the Darcy resistance drops out of the governing equations, and Eq. 1 reduces to the standard Navier-Stokes equations.

Resolvent analysis proceeds as follows. First, we employ a standard Reynolds-averaging procedure to determine the governing equations for the velocity and pressure fluctuations from Eq. 1 and the continuity constraint, $\nabla\cdot(\varepsilon\mathbf{u}) = 0$. Next, the governing equations for the fluctuations are Fourier-transformed and expressed as $[\mathbf{u_k}, p_\mathbf{k}]^T = H_\mathbf{k}\mathbf{f_k}$, in which the forcing $\mathbf{f_k}$ represents the nonlinear terms and $H_\mathbf{k}$ is the resolvent operator representing the linear forcing-response dynamics. A singular value decomposition of the discretized resolvent operator is then used to identify high-gain response and forcing modes (left-singular and right-singular vectors) as well as the forcing-response amplification (singular values) for a given wavenumber-frequency combination, $\mathbf{k}$.

For the remainder of this abstract, we focus on modes resembling the NW cycle (i.e., with $\mathbf{k}$ corresponding to $\lambda_x^+ = 10^3$, $\lambda_z^+ = 10^2$, and $c^+ = 10$) and consider the highest singular value as a measure of performance. If the singular value is reduced over the porous material (σ_p) relative to the smooth-wall value (σ_s), the porous material is likely to suppress the corresponding flow structure. We also test for the emergence of high-gain spanwise-constant rollers resembling Kelvin-Helmholtz vortices (i.e., with $\kappa_z = 0$) at the porous interface.

Numerical Implementation

Previous theoretical and numerical efforts have primarily considered a symmetric channel geometry, with porous materials at both the upper and lower walls (Rosti *et al.*, 2018; Gómez-de Segura *et al.*, 2018). However, this geometry would have limited optical access for Particle Image Velocimetry (PIV) in the laboratory experiments discussed below. Instead, we consider an asymmetric channel geometry corresponding to the experimental setup shown in Fig. 1(a). The fluid flow is unobstructed for $y \in [0, h]$ and the porous material occupies the region corresponding to $y \in (h, H+h)$, with $h = H$. We generate model predictions for $Re_\tau = u_\tau h/(2\nu) = 60$, which corresponds roughly to the conditions tested in the experiments, and for $Re_\tau = 180$, which corresponds to prior numerical simulations (Rosti *et al.*, 2018). Following standard convention, the half-height of the unobstructed region is used to define Re_τ. The spatially-homogeneous porous substrate is defined by its principal permeability components $\mathbf{K} = \mathrm{diag}(k_{xx}, k_{yy}, k_{zz})$. The porosity is set to $\varepsilon = 0.87$ to match the porosity of the materials tested in experiment.

No-slip boundary conditions are applied at the wall locations corresponding to $y = 0$ and $y = H + h$. The interface between the porous substrate and the unobstructed domain is located at $y = h$. The resolvent operator is discretized in the wall normal direction using the Chebyshev collocation method detailed by Aurentz & Trefethen (2017). This approach allows us to discretize the unobstructed and porous domains independently and couple these two domains through the jump boundary conditions proposed by Ochoa-Tapia & Whitaker (1995). The following boundary conditions are applied at the interface:

$$\mathbf{u}|_{y=h^-} = \mathbf{u}|_{y=h^+} \tag{2}$$

$$p|_{y=h^-} = p|_{y=h^+} \tag{3}$$

$$\left.\frac{\partial u}{\partial y}\right|_{y=h^-} = \frac{1}{\varepsilon}\left.\frac{\partial u}{\partial y}\right|_{y=h^+}, \quad \left.\frac{\partial w}{\partial y}\right|_{y=h^-} = \frac{1}{\varepsilon}\left.\frac{\partial w}{\partial y}\right|_{y=h^+} \tag{4}$$

Construction of the resolvent operator also requires a mean velocity profile, $U(y)$. The mean velocity is predicted from the Reynolds-averaged mean flow equation, with the Reynolds stress term modeled using an eddy viscosity. Specifically, we assume that the eddy viscosity within the porous substrate is zero. In the unobstructed zone, we use the analytic eddy viscosity profile developed by Reynolds & Tiederman (1967). For the model predictions presented in Fig.2 a total of 200 Chebyshev nodes are used for discretization in the wall normal direction. The nodes are divided evenly between the porous domain and the unobstructed domain. Further grid refinement beyond this point led to changes in singular values smaller than $O(10^{-4})$.

3D Printed Porous Materials

For this study, two custom anisotropic porous materials were fabricated using a stereo-lithographic 3D printer (formlabs Form 2) based on input from the resolvent-based predictions described below. The porous material microstructure consisted of a cubic lattice of rectangular rods with constant cross-section and varying spacing in the x, y, and z directions. Fabrication constraints (printing resolution, allowable unsupported lengths, resin drainage) limited the maximum anisotropy that could be achieved. The following two geometries represented a good compromise between reliable fabrication and anisotropy. The first case with spacings $s_x = 0.8$ mm and $s_y = s_z = 3.0$ mm contains larger pores facing the streamwise direction and small pores facing the wall-normal and spanwise directions. The second case with $s_x = s_z = 3.0$ mm and $s_y = 0.8$ mm contains larger pores facing the wall-normal direction. These materials are referred to as *x-permeable* and *y-permeable*, respectively. For both geometries, the rod cross-section was of size $d \times d$,

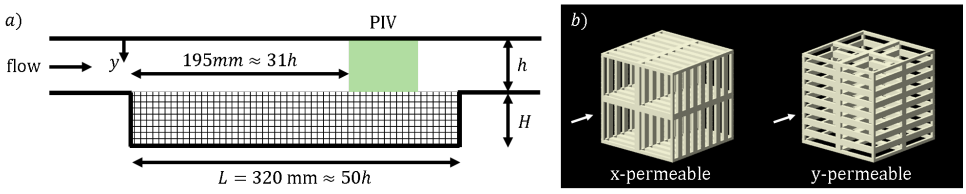

Figure 1. Schematic of the channel flow experiment (a) and porous material configurations (b); not to scale. The x-permeable case features large openings normal to the streamwise incoming flow. The y-permeable case has large openings in the wall-normal direction.

Table 1. Dimensionless permeability estimates for the 3D-printed porous materials. $H = 6.34$ mm is the height of the porous substrates tested in the channel flow experiments.

	ε	k_{xx}/H^2	k_{yy}/H^2	k_{zz}/H^2
x-perm	0.87	$4.3 \cdot 10^{-3}$	$5.5 \cdot 10^{-4}$	$5.5 \cdot 10^{-4}$
y-perm	0.87	$5.5 \cdot 10^{-4}$	$4.3 \cdot 10^{-3}$	$5.5 \cdot 10^{-4}$

with $d = 0.4$ mm. The porosity was $\varepsilon \approx 0.87$. The lattice structure for these substrates is shown in Fig.1(b).

Following Zampogna & Bottaro (2016), the permeability tensor ($\mathbf{K}$) for these anisotropic porous materials was determined by solving independent forced Stokes flow problems for a unit cell of the cubic lattice in the ANSYS Fluent software package. Due to the symmetric nature of the microstructures tested, only two Stokes flow problems were required to determine the permeability components k_{xx} and k_{yy}; k_{zz} is equal to either k_{xx} or k_{yy} depending on configuration (i.e., x-permeable or y-permeable). For these two Stokes flow problems, a uniform body forcing of unit amplitude was applied in the direction of the permeability component being evaluated. The permeability was determined from the resulting volume-averaged velocity using Darcy's law. Periodic boundary conditions were applied to the boundaries of the unit cell and a no-slip condition was applied at the solid boundaries. A time-marching scheme was used for each of these simulations. The solutions were determined to be at steady state when the residual in the permeability was less than 10^{-6}. A mesh independence study confirmed that our results were grid converged. The resulting permeability estimates are shown in Table 1. The anisotropic ratio is $\phi_{xy} = k_{xx}/k_{yy} \approx 8$ for the x-permeable case and $\phi_{xy} \approx 1/8$ for the y-permeable case.

Channel Flow Experiment

The anisotropic porous substrates described above were tested in a turbulent channel flow experiment, albeit at very low Reynolds number. A schematic of the experimental setup is shown in Fig. 1. A custom test section was machined from acrylic with a cutout of length $L = 320$ mm designed to hold the porous substrates. The width of the test section was $W = 50$ mm, and the height of the unobstructed region was $h = 6.34$ mm. The cutout was located approximately 150mm from the inflow, and allowed for 3D-printed tiles of thickness $H = h = 6.34$ mm to be mounted flush with the smooth wall upstream of the cutout. Note that the number of pores accommodated over the height of the tiles was limited to 2 for the x-permeable case and 8 for the y-permeable case, indicating limited separation between the pore-scale and outer-scale flow. For a baseline comparison, experiments were also carried out with a solid smooth-walled insert placed in the cutout.

Flow in the channel was generated using a submersible pump placed in a large water tank. The flow rate was controlled using an electronic proportioning valve. The volumetric flow rate was $Q = 92$ cm^3/s for the smooth wall and x-permeable cases, and $Q = 82$ cm^3/s for the y-permeable case. Thus, the bulk Reynolds number was $Re_b = Q/(W\nu) = 1840$ for the smooth wall and x-permeable case, and $Re_b = 1640$ for the y-permeable case. This corresponds to the lower end of the Re_b ranges considered by Suga *et al.* (2018) in recent experiments over anisotropic porous materials.

A 5W continuous wave laser with integrated optics was used to generate a laser sheet in the streamwise-wall normal direction at mid-span. A high-speed camera (Phantom VEO-410L) was used to capture images near the downstream end of the porous section. To provide an adequate development length (Efstathiou & Luhar, 2018), the field of view began 195mm ($\approx 31h$) from the leading edge of the porous section and extended 22mm ($\approx 3.5h$) downstream. Images were acquired at 2kHz for 10 seconds for a total of 20,000 images. The images were processed in PIVlab (Thielicke & Stamhuis, 2014) using the Fast-Fourier transform routine with a minimum box size of 16 pixels and 50% overlap, which yielded 36 (vertical) x 125 (horizontal) data points in the unobstructed section.

RESULTS

Model Predictions

Figure 2(a) shows the predicted change in singular values for resolvent modes resembling the NW cycle over anisotropic porous substrates as a function of their inner-normalized streamwise and wall normal permeabilities. Recall that the asymmetric channel geometry used for these predictions is similar to that tested in the experiments. Consistent with prior results, porous substrates with high streamwise permeability ($\sqrt{k_{xx}}^+$) and low wall-normal permeability ($\sqrt{k_{yy}}^+$) are found to suppress the NW cycle. Further, mode suppression increases as the permeability ratio increases, $\phi_{xy} \gg 1$. The predictions do not change substantially from $Re_\tau = 60$ (colored shading) to $Re_\tau = 180$ (solid black lines). In particular, the location of the neutral curve corresponding to $\sigma_p/\sigma_s = 1$ (i.e., no change in gain) is very similar for both Reynolds numbers.

For the specific porous materials tested in the experiments, the inner-normalized permeabilities correspond to $(\sqrt{k_{xx}}^+, \sqrt{k_{yy}}^+) = (7.9, 2.8)$ for the x-permeable case and $(\sqrt{k_{xx}}^+, \sqrt{k_{yy}}^+) = (2.8, 7.9)$ for the y-permeable case at $Re_\tau = 60$. These values were computed from the dimensionless permeabilities listed in Table 1 assuming $H^+ = 2Re_\tau = 120$. These specific permeability ratios are labeled

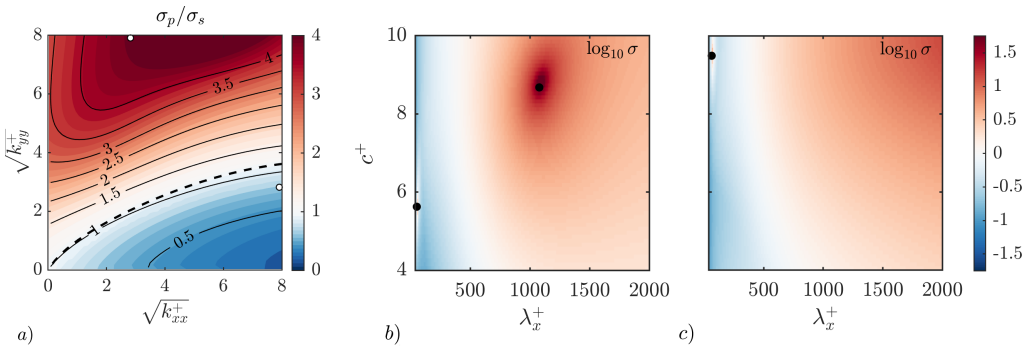

Figure 2. Panel (a) shows predicted singular value ratios (σ_p/σ_s) for resolvent modes resembling the NW cycle as a function of inner-normalized streamwise and wall-normal permeability. Results for $Re_\tau = 60$ are shown as colored contours. Solid black lines show results for $Re_\tau = 180$. Predictions shown for substrates defined by $\mathbf{K} = \mathrm{diag}(k_{xx}, k_{yy}, k_{yy})$. Panels (b) and (c) show amplification of spanwise-constant modes as a function of streamwise wavelength and mode speed at $Re_\tau = 60$ for the y-permeable and x-permeable substrates, respectively.

using ∘ markers in Fig. 2(a). Model predictions indicate that the x-permeable substrate suppresses resolvent modes resembling the NW cycle while the y-permeable substrate leads to further amplification. Previous studies show that NW cycle gain is a useful indicator of drag reduction performance with both active and passive control techniques (Luhar *et al.*, 2014; Chavarin & Luhar, 2018).

The appearance of large spanwise-constant structures resembling Kelvin-Helmholtz rollers is also expected over porous substrates (Breugem *et al.*, 2006; Chandesris *et al.*, 2013). Linear stability analysis and simulations performed by Gómez-de Segura *et al.* (2018) attribute the appearance of these structures to an increase in wall-normal permeability. Figures 2(b) and (c) show singular values for spanwise-constant resolvent modes over the y-permeable and x-permeable materials, respectively. A weak local maximum in gain is observed in both cases for small structures with $\lambda_x^+ \approx 50$. However, there is a much stronger local maximum in gain for structures with $\lambda_x^+ \approx 1100$ and $c^+ \approx 8.6$ over the y-permeable material (Fig. 2(b)). This additional local maximum does not appear for the x-permeable material, confirming that materials with higher $\sqrt{k_{yy}}^+$ are more susceptible to the emergence of large, high-gain spanwise rollers (see also Abderrahaman-Elena & García-Mayoral, 2017; Gómez-de Segura *et al.*, 2018).

Experimental Results

Fig. 3 shows the measured mean statistics for the channel flow experiments. These statistics were computed by averaging both in time and in the streamwise direction. Results in the region $y/h \geq 0.95$ were affected by reflections at the smooth/porous tiles and should be treated with caution. Fig. 3(a) shows that the mean profile remains relatively symmetric across the unobstructed region for the x-permeable material. However, for the y-permeable case, the bulk of the flow in the unobstructed region is shifted towards the smooth wall. The location of the maximum mean velocity was $y/h = 0.45$ for the x-permeable case and $y/h = 0.38$ for the y-permeable case. Interestingly, the slip velocity at the porous interface appears to be higher for the y-permeable case despite the substantially lower streamwise permeability. However, this observation could be attributed to the specific porous geometry tested here. As shown in Fig. 1(b), the porous interface is characterized by much lower *local* porosity for the x-permeable permeable compared to the y-permeable material. The visibly lower bulk-normalized mean profile for the x-permeable material in the unobstructed region is indicative of greater flow through the porous medium itself.

The Reynolds shear stress profiles in Fig. 3(b) show the presence of an (almost) linear region in the middle of the unobstructed domain. Friction velocities at the porous and smooth walls, u_τ^p and u_τ^s, were estimated by extrapolating from this linear region to $y = h$ and $y = 0$, respectively (see e.g., Breugem *et al.*, 2006). Note that the profiles shown in Fig. 3(b) are normalized by u_τ^s. With this normalization, it is clear that $u_\tau^p > u_\tau^s$ for both porous materials tested.

Actual friction velocity estimates are shown in Table 2. The x-permeable material does not lead to a significant change in friction velocities relative to the smooth wall case; u_τ^s values are nearly identical, and u_τ^p is higher by less than 20% for the x-permeable case. In contrast, the y-permeable material leads to a significant increase in friction velocities relative to the smooth-wall case; u_τ^s increases by 60% and u_τ^p by 110%. Thus, in contrast to the resolvent-based predictions, no reduction in friction is observed at the porous interface for the x-permeable material. The y-permeable material leads to a *substantial* increase in friction at both the smooth wall and the porous interface. This is qualitatively consistent with model predictions, which show a substantial increase in NW cycle gain as well as the emergence of high-gain spanwise rollers over the y-permeable material.

Table 2. Friction velocity estimates at the smooth wall (u_τ^s) and porous interface (u_τ^p). *For the smooth wall case u_τ^p corresponds to the solid tile placed in the cutout.

Case	u_τ^s [m/s]	u_τ^p [m/s]
smooth wall	0.0154	0.0165*
x-permeable	0.0152	0.0193
y-permeable	0.0247	0.0346

Figs. 3 (c) and (d) show profiles for the root-mean-square streamwise velocity fluctuations normalized by u_τ^s and u_τ^p, respectively. When normalized by u_τ^s, the near-wall peaks on the smooth wall side collapse together for all cases. At the porous interface, the peaks for the smooth

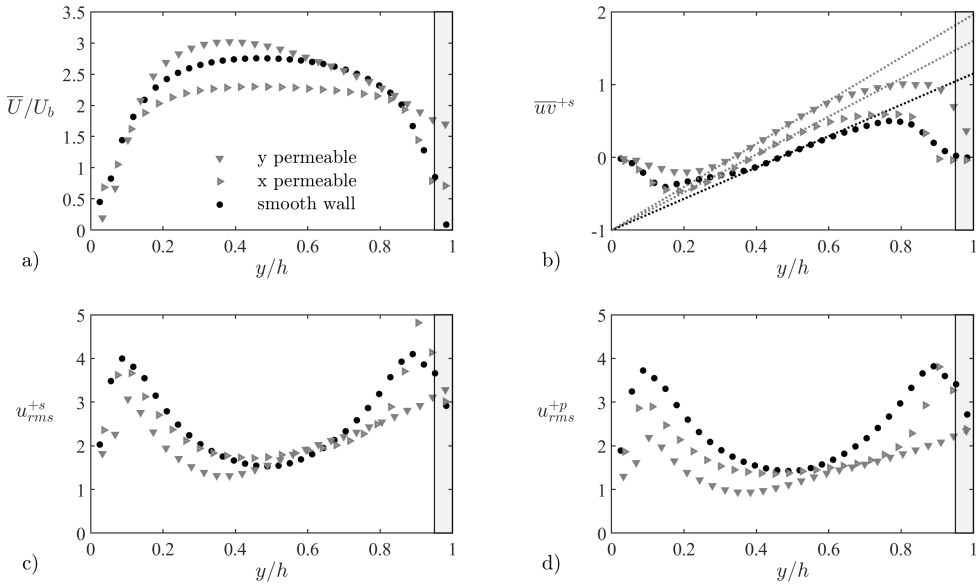

Figure 3. PIV results for the channel flow experiment. The smooth wall is located at $y = 0$, while the interchangeable wall is located at $y = h$. Panel (a) shows the measured mean velocity profiles normalized by the bulk-averaged velocity (calculated using $H + h$ in all cases). Panel (b) shows Reynolds shear stress profiles normalized by the smooth-wall friction velocity. Note that friction velocities at the smooth and porous walls were estimated by extrapolating the linear region in the Reynolds shear stress profile to the wall locations. Panels (c) and (d) show profiles of the root-mean-square streamwise fluctuations normalized by the smooth wall and porous wall friction velocities (u^s_τ and u^p_τ) respectively.

wall and x-permeable case collapse when normalized by u^p_τ, indicating that the flow physics are qualitatively similar for these substrates. However, the profile for the y-permeable case has no discernible peak near the porous interface, and the magnitude of u^+_{rms} is lower. This observation is consistent with previous results (Breugem *et al.*, 2006; Suga *et al.*, 2018), and is indicative of a change in flow structure.

Proper Orthogonal Decomposition

To provide further insight into the changes in mean statistics discussed above, proper orthogonal decomposition (POD) was performed on the fluctuating velocity fields obtained from PIV. The streamwise velocity fields associated with the first 2 spatial modes for the smooth wall, x-permeable, and y-permeable cases are shown in Fig. 4. As expected, the most energetic modes for the smooth wall case resemble long streaky structures that are symmetric across the channel.

The first POD mode for the x-permeable case suffers from some distortion and does not have a clear physical interpretation. However, the second mode closely resembles the first mode for the smooth wall case. The streamwise extent of the plots shown in Fig. 4 corresponds to the PIV field of view, which is roughly $3.5h$ or 22 mm. With this in mind, the first smooth-wall mode and the second x-permeable mode appear to have a streamwise wavelength that is more than twice the PIV field of view, $\lambda_x > 44$ mm (or $\lambda_x > 7h$). For the friction velocity estimates shown in Table 2, this translates into $\lambda_x^+ > 700$, which is consistent with the scale of NW streaks (Robinson, 1991).

Unlike the smooth-wall and x-permeable cases, POD modes for the y-permeable material have a visibly asymmetric structure in the wall-normal direction. For both modes, the streamwise velocity field is much more intense near the porous interface. Moreover, the full velocity field for these POD modes (wall-normal component not shown here) is indicative of a counter-rotating structure. Such rollers have been observed in previous numerical simulations (Breugem *et al.*, 2006), and are typically associated with a Kelvin-Helmholtz instability mechanism. This observation provides qualitative support for the model predictions shown in Fig. 2(b), which show that the y-permeable material is susceptible to the emergence of large high-gain spanwise constant structures. More quantitatively, the first POD mode over the y-permeable material appears to have a streamwise wavelength of roughly twice the PIV field of view, $\lambda_x \approx 7h \approx 44$ mm. Using the u^p_τ estimate shown in Table 2, this yields $\lambda_x^+ \approx 1500$, which is larger than the streamwise wavelength predicted for the high-gain spanwise roller in Fig. 2(b), $\lambda_x^+ \approx 1100$.

DISCUSSION

Consistent with previous studies and model predictions, the present experiments show a very different flow response over the x-permeable and y-permeable materials. The x-permeable material leads to a marginal increase in friction velocity at the porous interface (Fig. 3(b)). This is counter to resolvent-based predictions, which suggest that the x-permeable material should lead to a reduction in gain for the NW cycle (Fig. 2(a)). Possible explanations for this discrepancy include: the emergence of small-scale spanwise rollers, as predicted by the resolvent formulation; roughness effects at the porous interface that are neglected in the VANS equations; nonlinear (Forchheimer) effects becoming important in the porous medium; and perhaps most importantly, insufficient scale separation between the pore-scale and outer flow. The y-permeable material leads to a significant increase in friction velocities at both walls relative to the smooth wall and x-permeable cases. This is consistent with resolvent-based predictions, which indicate a substantial increase in NW cycle gain as well as the emergence of large, high-gain spanwise rollers over the y-

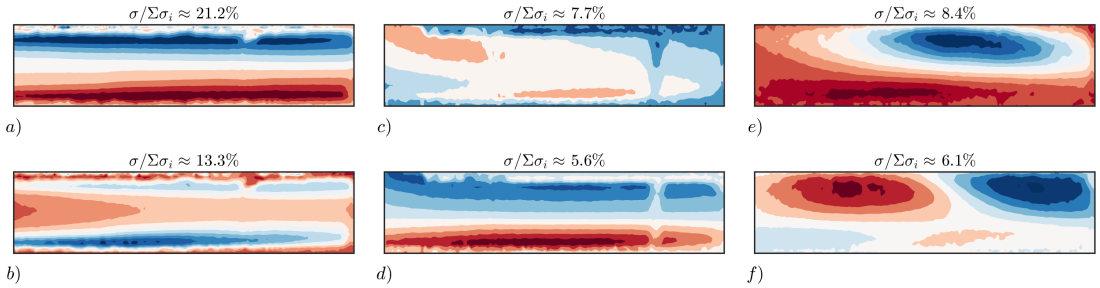

Figure 4. The first two POD modes for the smooth wall case (a,b), x-permeable case (c,d) and the y-permeable case (e,f). The modes are computed using 20,000 PIV frames. Contours show normalized levels for the streamwise velocity component. The porous interface is at the top wall.

permeable material. POD confirms the presence of such spanwise rollers over the y-permeable material (Fig. 4). However, the streamwise length-scale for the first POD mode is larger than the wavelength for the highest-gain roller identified via resolvent analysis. This lack of quantitative agreement could be due to the mean profile used in the resolvent operator. Predictions made using the eddy viscosity model yield a mean profile that deviates significantly from the asymmetric profile shown in Fig. 3a.

Together the model predictions and experimental results shown here confirm that materials with high streamwise permeability and low spanwise and wall-normal permeability are good candidates for drag reduction. Ongoing work seeks to alleviate some of the weaknesses associated with the current experimental setup (limited development length, insufficient scale separation, low Reynolds number) and to identify streamwise-permeable porous materials that could be more effective.

ACKNOWLEDGEMENTS

This material is based on work supported by the Air Force Office of Scientific Research under award FA9550-17-1-0142 (program manager Dr. Gregg Abate).

REFERENCES

Abderrahaman-Elena, Nabil & García-Mayoral, Ricardo 2017 Analysis of anisotropically permeable surfaces for turbulent drag reduction. *Phys. Rev. Fluids* **2**, 114609.

Aurentz, J. & Trefethen, L. 2017 Block operators and spectral discretizations. *SIAM Review* **59** (2), 423–446.

Breugem, WP, Boersma, BJ & Uittenbogaard, RE 2006 The influence of wall permeability on turbulent channel flow. *Journal of Fluid Mechanics* **562**, 35–72.

Chandesris, Marion, d'Hueppe, A, Mathieu, Benoit, Jamet, Didier & Goyeau, Benoit 2013 Direct numerical simulation of turbulent heat transfer in a fluid-porous domain. *Physics of Fluids* **25** (12), 125110.

Chavarin, Andrew & Luhar, Mitul 2018 Resolvent analysis for turbulent channel flow with riblets. *arXiv preprint arXiv:1812.07178* .

Choi, Haecheon, Moin, Parviz & Kim, John 1993 Direct numerical simulation of turbulent flow over riblets. *Journal of fluid mechanics* **255**, 503–539.

Efstathiou, Christoph & Luhar, Mitul 2018 Mean turbulence statistics in boundary layers over high-porosity foams. *Journal of Fluid Mechanics* **841**, 351–379.

Garcia-Mayoral, Ricardo & Jimenez, Javier 2011 Hydrodynamic stability and breakdown of the viscous regime over riblets. *Journal of Fluid Mechanics* **678**, 317–347.

Lee, S-J & Lee, S-H 2001 Flow field analysis of a turbulent boundary layer over a riblet surface. *Experiments in fluids* **30** (2), 153–166.

Luchini, Paolo, Manzo, Fernando & Pozzi, Amilcare 1991 Resistance of a grooved surface to parallel flow and cross-flow. *Journal of fluid mechanics* **228**, 87–109.

Luhar, Mitul, Sharma, Ati S & McKeon, Beverley J 2014 Opposition control within the resolvent analysis framework. *Journal of Fluid Mechanics* **749**, 597–626.

McKeon, B. J. & Sharma, A. S. 2010 A critical-layer framework for turbulent pipe flow. *Journal of Fluid Mechanics* **658**, 336–382.

Ochoa-Tapia, J Alberto & Whitaker, Stephen 1995 Momentum transfer at the boundary between a porous medium and a homogeneous fluidi. theoretical development. *International Journal of Heat and Mass Transfer* **38** (14), 2635–2646.

Reynolds, W. C. & Tiederman, W. G. 1967 Stability of turbulent channel flow, with application to malkus's theory. *Journal of Fluid Mechanics* **27** (2), 253–272.

Robert, JP 1992 Drag reduction: an industrial challenge. *Tech. Rep.*. AIRBUS INDUSTRIE BLAGNAC (FRANCE).

Robinson, Stephen K 1991 Coherent motions in the turbulent boundary layer. *Annual Review of Fluid Mechanics* **23** (1), 601–639.

Rosti, Marco E, Brandt, Luca & Pinelli, Alfredo 2018 Turbulent channel flow over an anisotropic porous wall–drag increase and reduction. *Journal of Fluid Mechanics* **842**, 381–394.

Gómez-de Segura, Garazi, Sharma, Akshath & García-Mayoral, R 2018 Turbulent drag reduction using anisotropic permeable substrates. *Flow, Turbulence and Combustion* **100** (4), 995–1014.

Suga, Kazuhiko, Okazaki, Yuki, Ho, Unde & Kuwata, Yusuke 2018 Anisotropic wall permeability effects on turbulent channel flows. *Journal of Fluid Mechanics* **855**, 983–1016.

Thielicke, William & Stamhuis, Eize J. 2014 Pivlab towards user-friendly, affordable and accurate digital particle image velocimetry in matlab. *Journal of Open Research Software* **2**.

Walsh, M & Lindemann, A 1984 Optimization and application of riblets for turbulent drag reduction. In *22nd Aerospace Sciences Meeting*, p. 347.

Zampogna, Giuseppe A. & Bottaro, Alessandro 2016 Fluid flow over and through a regular bundle of rigid fibres. *Journal of Fluid Mechanics* **792**, 5–35.